

## Water-Induced Reconstruction that Affects Mobile Ions on the Surface of Calcite

Trevor A. Kendall<sup>†</sup> and Scot T. Martin\*

Division of Engineering and Applied Sciences, 29 Oxford Street, Harvard University, Cambridge, Massachusetts 02138

Received: July 24, 2006; In Final Form: October 30, 2006

Time-sequenced contact-force micrographs show that the (10̄14) calcite cleavage surface reconstructs in humid air through pit formation and film growth. After 8 h at 80% relative humidity (RH), 50% to 80% of the surface is covered by islands that are flat-topped and 1-nm high. The lateral growth rates of individual islands are  $4.2 \pm 0.4 \text{ nm min}^{-1}$  in the 4̄41 direction and  $1.8 \pm 0.4 \text{ nm min}^{-1}$  in the 48̄1 direction, resulting in islands having distinct major and minor axes. On some samples, a contiguous, 1.5-nm-high film rapidly grows between the islands and the pits. The areal expansion rate of the film is 500 times faster than that of the islands. Gaps between the contiguous film and the islands expand and contract, which suggests that mass is exchanged between them and that both are loosely bound. Complementing the topographic images, polarization heights are simultaneously measured by polarization-force microscopy. The polarization heights of the islands and the contiguous film are  $-6$  to  $-10 \text{ nm}$  and  $-4$  to  $-5 \text{ nm}$ , respectively, compared to their respective topographic heights of  $+1.0$  and  $+1.5 \text{ nm}$ . Under our experimental conditions, the polarization heights are a surrogate for the local dielectric constant of the sample  $\epsilon$  and arise from a convolution of the mobility and the density of surface ions. The polarization heights imply that  $\epsilon_{\text{substrate}} > \epsilon_{\text{film}} > \epsilon_{\text{island}}$ . Changes in topographic and polarization heights at 20% and 50% RH suggest that the structures of the islands are in dynamic equilibrium with the adsorbed water. Our evidence suggests that the islands contain loosely bound water and may therefore be a hydrated calcium carbonate phase stabilized by the calcite surface.

### Introduction

Calcium carbonate minerals, which include calcite, aragonite, vaterite, and an amorphous form, constitute the skeletal parts of mollusks, crustaceans, and many other life forms,<sup>1</sup> regulate the pH of many natural waters,<sup>2</sup> and serve as construction materials for society.<sup>3</sup> Cycles of relative humidity in the atmosphere, of the water table below ground, and of precipitation at the Earth's surface lead to the drying and rewetting of carbonate mineral surfaces in soils,<sup>4</sup> biominerals,<sup>5</sup> and atmospheric particles.<sup>6,7</sup> Reversible and irreversible changes in the molecular and physical features of the surface and hence in surface reactivity accompany the cycling of the layer thickness of adsorbed water during drying and rewetting. The surface reconstruction is driven by a minimization of energy in response to a perturbation.<sup>8</sup> Water sorption, for example, leads to surface hydrolysis (such as  $-\text{OH}$  and  $-\text{H}$  terminated calcite surface groups), to the solvation and the mobilization of surface ions, and to changes in physical features such as steps or pits.<sup>9–12</sup> For example, Stipp et al. qualitatively documents physical features forming on calcite in humid air.<sup>11</sup> The processes that form these features, however, remain incompletely understood. In particular, the behavior of mobile surface ions is greatly affected by and, in turn, greatly affects surface reconstruction and reactivity,<sup>9</sup> although quantitative connections are lacking.

Surface ions are characterized by density  $\sigma$  and mobility  $\mu$ , among other properties. The density of mobile surface ions is affected by the many locations of potential energy minima such

as binding sites, which are in turn influenced by the properties and the quantity of adsorbed water.<sup>8,13</sup> The mobility of an ion on a solvated surface is regulated by diffusional, mechanical, and electrical properties distinct from the better-understood counterparts of bulk solution. Surface mobility is affected by interactions with physical surface features such as steps and pits, as well as the solvating properties of the water layer on the surface. Mobile surface ions have a dominant two-dimensional component to their motion.

The density and the mobility of surface ions can be probed experimentally by using electric fields. In this approach, heterogeneities in  $\sigma$  and  $\mu$  on the surface are mathematically subsumed as a local dielectric constant  $\epsilon$ ,<sup>14,15</sup> notwithstanding that the processes of ion release to a surface water layer and the mobility within a water layer are incompletely understood and that atomistic modeling of these processes remains a formidable challenge.

Scanning polarization-force microscopy (SPFM) allows spatially resolved measurements of the local dielectric constant (i.e., the response of mobile surface ions).<sup>14,15</sup> Previous studies employing SPFM led to an improved understanding of dissolution and ion sorption by linking the behavior of mobile ions to surface reconstruction.<sup>9,16,17</sup> The current study investigates the role of mobile ions in island and film overgrowth accompanying surface reconstruction. Calcite is the mineral selected for study. The observations show a tight coupling between the progress of reconstruction and the behavior of mobile surface ions.

### Experimental Section

**Protocol Overview.** Freshly cleaved calcite surfaces were imaged by atomic force microscopy (AFM) for up to 10 h.

\* To whom correspondence should be addressed. E-mail: smartin@deas.harvard.edu; www.deas.harvard.edu/environmental-chemistry.

<sup>†</sup> Current address: Clemson University, School of the Environment, 340 Brackett Hall, Clemson, SC 29634-0919.

Experiments were begun just after cleaving a sample. The relative humidity inside the AFM chamber was controlled and set to 80% for most of the experiments. Experiments were concluded once extensive surface reconstruction had occurred. Polarization-height and contact-mode images were collected in succession in intervals of 30 to 60 min, from which measurements of polarization and topographic heights were respectively obtained.

**Sample Preparation.** Single crystals of Iceland Spar calcite (Chihuahua, Mexico) were purchased from Ward's Geology (Rochester, New York). Fresh (1014) surfaces were prepared by cleaving the samples with a sharp razor blade at ambient relative humidity, which ranged from 40% to 60%. Sample surfaces were swept with a stream of ultrapure nitrogen to remove loose material that sometimes accumulated during and after cleavage. Samples were secured with silver paste (SPI, Inc., West Chester, PA) to an AFM mounting disk to ensure good electrical conductivity between the mineral surface and the mount.

**Relative Humidity Control.** The relative humidity (RH) surrounding the sample was controlled by flowing dry nitrogen and water vapor into an acrylic environmental chamber that housed the atomic force microscope. The proportionated flows were thoroughly mixed before entering the environmental chamber, which was sealed with rubber o-rings and maintained under continuous positive pressure. The relative humidity inside the chamber was adjusted prior to sample insertion. Relative humidity and temperature were respectively monitored by a capacitive water sensor (HC 610, Ohmic Instruments Co., Easton, MD, 2% accuracy) and a thermistor (Omega 44033, Stamford, CT, 0.1 °C accuracy), both of which were placed near the sample surface. The RH sensor was periodically calibrated using saturated solutions of LiCl (11% RH), NaCl (75% RH), and KNO<sub>3</sub> (93% RH). Experiments were performed at room temperature and typically at 80% RH. Relative humidity and temperature data were recorded using a stripchart module within a customized code in the software package *Igor* (WaveMetrics, Inc., Lake Oswego, OR).

**Scanning Polarization-Force Microscopy.** Scanning polarization-force microscopy (SPFM) is a noncontact imaging mode of traditional atomic force microscopy (Figure 1).<sup>18</sup> A voltage-biased tip, located tens to hundreds of nanometers from a surface, induces an image charge and thereby establishes a polarization force between the tip and the sample surface. Under the conditions of our study at 80% RH, this image charge arises almost entirely from mobile surface ions.<sup>17,18</sup> SPFM can be used on insulating surfaces, including carbonate minerals.<sup>9</sup> A detailed description of the principles and of the implementation of polarization-force measurements is provided elsewhere.<sup>15,18</sup> The instrument description here focuses on our adaptation of a commercial system for application to SPFM.

**Adaptation of a Commercial Instrument.** Scanning polarization-force microscopy was adapted to a Digital Instruments NanoScope IIIa Multimode Scanning Probe Microscope (SPM) having a signal access module (SAM; model SBOB-1). Conductive Pt-coated Si<sub>3</sub>N<sub>4</sub> tips (Nanosensors, Inc.) were employed, and the specific value of the force constant *k* of the cantilever (ranging from 0.12 to 0.40 N m<sup>-1</sup>) for each batch of tips was provided by the manufacturer. A dc bias of -3.0 V was applied to a tip by connecting the "ANA2" input port of the SAM to a function generator (Agilent Technologies Inc., model 33120A, Palo Alto, CA). An insulated tip holder (Digital Instruments, model no. MMEFCH) was employed to ensure that the bias applied to the tip did not short. The polarization force between

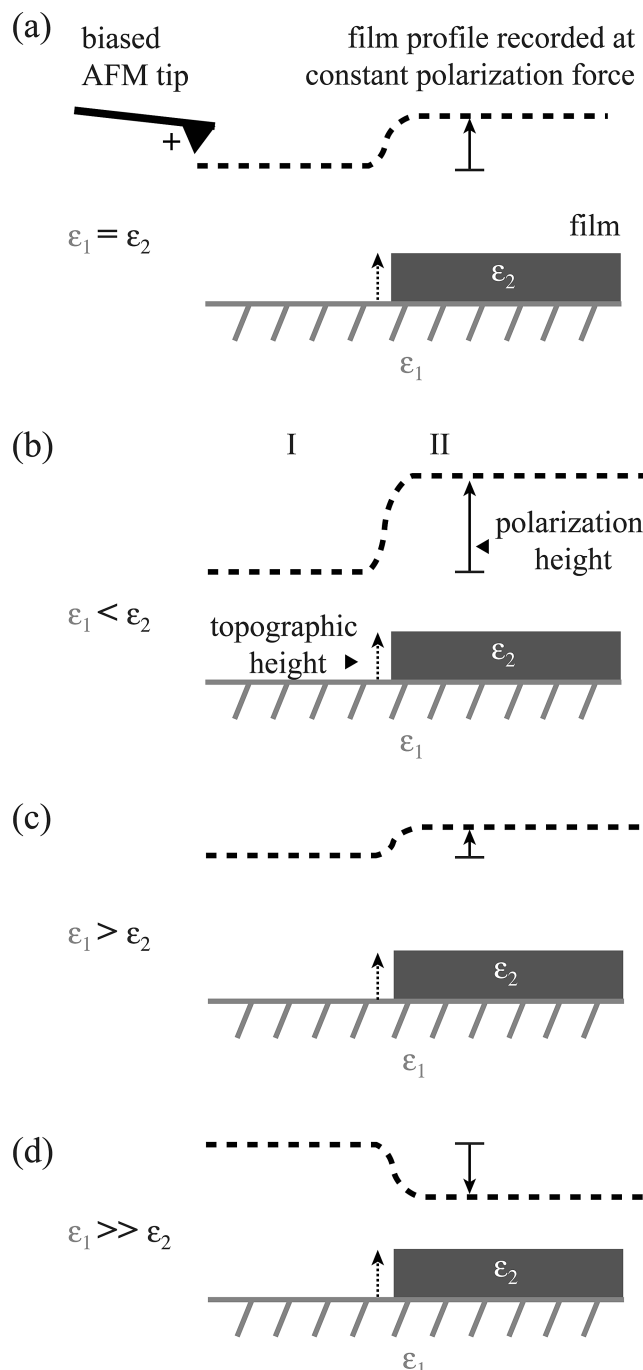


**Figure 1.** Scanning polarization-force microscopy. A constant polarization force is maintained between the biased tip and the sample during imaging by adjusting the tip-sample separation. Cases *a* through *d* show the cross sections of the polarization height. The topographic heights are the same in *a* through *d*, and the local contact potential is 0 V everywhere. (*a*) If the dielectric constants  $\epsilon$  of the film and the substrate are equal, then the polarization height has exact fidelity with the topographic contour. (*b*) The polarization height is larger than the topographic height for  $\epsilon_1 < \epsilon_2$ . Over region I, the tip is tensioned by a polarization force equal to the setpoint force, thereby establishing a zero baseline for the polarization height. Over region II, the polarization force increases because  $\epsilon_1 < \epsilon_2$ . As a result, the setpoint force is restored only by increasing the tip-sample separation. The polarization height is then greater than the topographic height for  $\epsilon_1 < \epsilon_2$ . Similar thinking explains the polarization profiles illustrated in *c* and *d* for  $\epsilon_1 > \epsilon_2$  and  $\epsilon_1 >> \epsilon_2$ , respectively. Case *d* shows that a negative polarization height is possible even over a region of positive topographic height. (For clarity of presentation, the diagram suggests that the tip is moving up-down, although the surface is moving up-down on the piezoelectric scanner in the actual apparatus.)

the dc-biased tip and the sample surface was attractive, causing the tip to deflect downward when near the surface (eq 1a). The mechanical deflection of the tip in response to the polarization force was recorded by the photodiode in the optical head of the SPM, and the voltage from the photodiode was conveyed to the control computer running the software supplied by Digital Instruments.

“Contact mode”, a normal operating mode of the software, was employed, although the values of several of the control parameters were adjusted, as follows. (1) The downward deflection caused by the attractive polarization force as the tip neared the surface was the opposite of the upward deflection that occurred in contact imaging, for which the tip was pressed against the surface. To invoke a feedback loop within the commercial software, we set the “detector sensitivity” to  $-1 \text{ nm/V}$ . For comparison, this value was  $+1 \text{ nm/V}$  in the usual mode of contact imaging. (2) The tip was coarsely “autoengaged” using a target setpoint (entered into the software) of 0.01 to 0.12 V less than the value of  $(A - B)/(A + B)$  displayed on the AFM base. Fine adjustment to the tip–sample separation then followed by decreasing the setpoint in steps of 0.001 to 0.010 V until the difference between the trace and the retrace in a scan line was minimized. (3) The “setpoint” of constant polarization force ranged from 0.7 to 10 nN (50 to 5 nm tip–sample separation) for a tip bias of  $-3.0 \text{ V}$ . (4) The “interval” and “proportional” gains were typically set to 7.0 and 9.0, respectively. (5) Images of 0.5- to 5- $\mu\text{m}$  wide were collected at a “line scan rate” of 1.1 Hz.

Using these software settings, we collected polarization images in the “contact mode” of the software. Namely, piezoelectric height positions required to maintain a constant polarization force were obtained by feedback control of the tip–sample separation while a two-dimensional in-plane raster scan was performed. False-color images were prepared from the heights recorded during the raster scan. Height data were also processed using *WSxM 4.0 Develop 8.0* (Nanotec Electrónica, Madrid, Spain).

To be clear, contact-mode images of traditional AFM and operating the software in “contact mode” to collect polarization images were distinct.

*Interpretation of the Measurements.* In their most general form, polarization images are a convolution of the local topography, the local dielectric constant of the sample surface, and the local contact potential between the tip and the sample. For our experimental conditions at 80% RH of a hydrated, microscopically flat ionic surface, however, the contribution by the local dielectric constant is dominant. Further explanation of this simplification is provided below, and experimental evidence of its accuracy is given in the section on local dielectric constant  $\epsilon(\hat{p})$ .

The baseline of zero height in a polarization image is established by engaging the tip at a setpoint dc-polarization force (described by eq 1a). Image contrast of nonzero polarization height  $z$  results when the tip is raster scanned in position  $\hat{p}$ , representing the  $x$ – $y$  location over the surface. The tip deflection (i.e., the polarization height) is related by Hook’s law to the polarization force  $F$  that acts on the cantilever (i.e.,  $F = -kz$ ). Equation 1a (see below) shows the factors affecting the magnitude of this force.<sup>15</sup> Equation 1b shows the factors modulating the force and thus provides image contrast for the case that  $\partial_\epsilon F$  is much greater than  $\partial_z F$  and  $\partial_\varphi F$  as the tip is scanned in  $\hat{p}$ . For the high concentration of mobile surface ions at 80% RH, the contribution of  $\partial_\varphi F$  is small compared to the dielectric term  $\partial_\epsilon F$ . Moreover, the surfaces studied are flat (e.g.,

as demonstrated by the contact-mode images) so that  $\partial_\epsilon F$  is generally much greater than  $\partial_z F$ . The related implication is that the relative variation of the local dielectric constant  $\partial_{\hat{p}}\epsilon$  greatly exceeds that of the local contact potential  $\partial_{\hat{p}}\varphi$  and that of the local topography  $\partial_{\hat{p}}z$ .

The equations are as follows:

$$F = -4\pi\epsilon_0 \cdot \frac{\epsilon - 1}{\epsilon + 1} \cdot f\left(\frac{R}{d}\right) \cdot (V - \varphi)^2 \quad (1a)$$

$$\partial_\epsilon F = -8\pi\epsilon_0 \cdot f\left(\frac{R}{d}\right) \cdot \frac{(V - \varphi)^2}{(\epsilon + 1)^2} \quad (1b)$$

where  $\epsilon$  is the local dielectric constant,  $d$  is the tip–sample separation,  $R$  is the tip radius,  $f(R/d)$  is a geometry function depending on the shape of the tip and of the local surface,  $V$  is the bias voltage applied to the tip, and  $\varphi$  is the local contact potential. The local contact potential arises from the voltage drop from the tip to the sample because of fixed surface charges. Equation 1a shows that the polarization force is negative (i.e., attractive). The mechanical-force response time of the tip is instantaneous compared to the polarization-force response time of the ions. Therefore, there is no phase lag between the tip position and the force indicated by eq 1a, and the polarization force is an instantaneous measure of the local values of the terms in eq 1a.

Under the conditions of our study at 80% RH and for our operating protocols of SPFM, the dominant contribution to image contrast is the variation in the local dielectric constant  $\partial_{\hat{p}}\epsilon$ . For a heterogeneous surface, the ratio  $v\tau/l$  determines whether the tip response represents the local environment of the surface or is instead affected by nearby heterogeneities, where  $v$  is the tip speed (typically  $11 \mu\text{m s}^{-1}$  in our application),  $\tau$  is the polarization-force response time (10 to 30 ms in most of our studies, as reported in Kendall and Martin<sup>9</sup>), and  $l$  is the lateral scale of a surface region having altered ion-mobility properties.<sup>17,18</sup> The terms  $\tau$  and  $l$  both vary with  $\hat{p}$ . For  $v\tau/l$  of unity, there is approximately a one e-fold response in the positions of the mobile ions toward a dc-biased tip and hence of the tip toward the equilibrium tension force that is reached when all ions have sufficient time to reach their steady-state positions. When the condition  $v\tau/l < < 1$  can be satisfied for features in an image, interpretation is greatly simplified because the tip response is affected only by the features directly beneath it (see further in section on Local Dielectric Constant  $\epsilon(\hat{p})$ ).

Figure 1 shows how changes in the dielectric properties of a film overlying a substrate affect the polarization height of the film. Equation 1b, for example, shows that a film having a dielectric constant greater than the substrate (i.e.,  $\partial_{\hat{p}}\epsilon > 0$ ) experiences an increased attractive polarization force, thereby requiring the piezoelectric scanner to retract to maintain the setpoint force established over the substrate. Retraction is interpreted as increased height in “contact mode”. In short, the polarization height exceeds the topographic height for the described conditions. A further description of the relationship between polarization and topographic heights is provided by Xu and Salmeron.<sup>15</sup>

Although we report only on dc imaging, in principle, the dielectric constant depends on the frequency of the voltage applied to the tip because of the frequency-dependent polarization response of mobile surface charges. Xu and Salmeron<sup>15</sup> report on the capabilities and limitations of imaging using an ac bias applied to the tip.

**Contact-Mode Imaging.** Contact-mode images were collected for comparison with the polarization images. The SPFM

tip was also used in contact mode so that the imaging modes could be interleaved. Wear of the Pt coating was a possibility during contact imaging; however, control experiments showed no effect of contact imaging on polarization-force measurements (data not shown). The control parameters for the contact-mode images were a “detector sensitivity” of +1 nm/V, a “setpoint” of 10 nN, “interval” and “proportional” gains typically of 4.0 and 6.0, respectively, and a “line scan rate” typically of 2.1 Hz. Alterations of the calcite surface because of tip contact were minimized by the weak “setpoint” force and the slow “line scan rate”. Periodically, the scan area was expanded, and an image was collected to confirm the absence of displaced material at edges of the smaller experimental scan area.

## Results and Discussion

**Surface Morphology.** At 80% relative humidity, freshly cleaved calcite terraces reconstruct during a 10-h period (Figure 2). Three mechanisms of reconstruction are operative: (1) the nucleation and the growth of individual islands, (2) the lateral expansion and the vertical deepening of pits, and (3) an abrupt event of the rapid growth of a contiguous film. Island and pit growth are observed for every sample (Figure 2a–c). The rapidly growing and contiguous film, however, occurs as an abrupt event in only 6 of the 10 samples (Figure 2d). Movies of time-sequenced micrographs showing the reconstruction of the calcite surface are included as Supporting Information.

The consistent orientation and morphology of the islands and the pits and the tight distribution of their respective topographic heights and depths suggest that crystallographic forces direct aspects of reconstruction (Figure 3). The islands are flat-topped. The average and  $2\sigma$  standard deviation of the distribution of topographic heights are 1.0 and 0.2 nm, respectively, based on 30 islands across 5 calcite samples.

Although the island edges are irregularly shaped in the lateral plane, a major axis of orientation is apparent. The major axis is oriented parallel to the  $\bar{4}41$  direction of calcite. (Our labeling of directions follows that of Morse and Arvidson.<sup>19</sup>) Growth occurs anisotropically and in two specific lateral directions perpendicular to one another (Figure 3). The lateral growth rates of individual islands are  $4.2 \pm 0.4 \text{ nm min}^{-1}$  in the  $\bar{4}41_{\text{obtuse}}$  direction and  $1.8 \pm 0.4 \text{ nm min}^{-1}$  in the  $48\bar{1}_{\text{acute}}$  direction, where “obtuse” and “acute” refer to the angle at which pit walls intersect the (1014) surface.<sup>12,19</sup> The lateral growth rates are calculated by measuring the distance between a fixed point, such as surface debris or a tip indentation, and the island edge. The lateral dimensions increase at these rates until termination by edge–edge coalescence or encountering a mono- or multilayer step. The average areal growth rate of the islands is  $1570 \pm 137 \text{ nm}^2 \text{ min}^{-1}$ , as calculated by use of the particle analysis module of *Igor*. Calculations are based on 60 observations over 4 calcite samples. Uncertainties are given for a 95% confidence interval.

Nucleation and growth continues throughout the time course of observations as long as bare substrate surface remains. Individual islands form from clusters of 5- to 10-nm width and 0.5- to 0.7-nm height. The heights increase until reaching a 1-nm limit. The total number of individual islands increases until coalescence begins.

Amidst the islands, elongated pits form after 60 to 120 min. The pits are oriented at  $35^\circ$  relative to the major axis of the islands. The averages of the distributions of width, length, and depth are 50, 143, and 0.40 nm, respectively, for a set of 10 observations. The corresponding  $2\sigma$  standard deviations are 12, 80, and 0.09 nm. New pits continually form throughout the

experiment, and the total number of pits increases with time. After 200 to 300 min, the distribution of pit dimensions changes to  $63 \pm 22 \text{ nm wide}$ ,  $350 \pm 50 \text{ nm long}$ , and  $0.52 \pm 0.12 \text{ nm deep}$ . Comparison of the data from 60 to 120 min to those from 200 to 300 min shows that the pits expand most rapidly along the long axis. The length-to-width ratio, for example, increases from 2.9 to 5.6.

In an abrupt event (cf. Figure 2c and d), a contiguous film rapidly grows in 6 of the 10 samples and subsequently covers the initial surface, excluding regions having pits or islands. The topographic height of the film is  $1.50 \pm 0.13 \text{ nm}$  (average and  $2\sigma$  standard deviation of 30 observations). The film lacks apparent crystallographic orientation relative to the substrate, and the lateral growth rate of the film is isotropic, corresponding to an approximate areal expansion rate of  $9 \times 10^5 \text{ nm}^2 \text{ min}^{-1}$ . This areal expansion rate is 500 times faster than that of the islands. A source of the mass for the film appears to be residual nanoparticles remaining after cleavage and preparation. Figure 4 shows an example of the film growing outward from a nanoparticle. Stipp et al. report a similar observation that film growth is associated with residual particles.<sup>11</sup> No rationalization is offered by us to explain the absence of abrupt film growth in 4 of 10 cases except to note that the film may form but remain outside of the scan area.

The contiguous film is dynamic. Gaps in the film expand and contract, and new gaps occasionally nucleate (see Supporting Information S1 and S2). The implication could be that the material of this film is loosely bound (see section on Proposed Chemical Composition of Islands). Island nucleation and growth occurs within newly formed gaps, and in some cases, islands appear to grow at the expense of the film, an observation which could suggest that mass is exchanged between the islands and the film in an example of Ostwald ripening.<sup>20</sup>

To assess the possibility that surface reconstruction is induced by the tip during contact imaging, we occasionally collect scans several hundreds of microns away from the locations where the time series of images is collected. Reconstruction features similar to those shown in Figure 2 are also apparent in the images from these distant locations. This check against tip-induced features is conducted at multiple time points throughout the 10-h experiment.

**Local Dielectric Constant  $\epsilon(\hat{p})$ .** The polarization heights approach a limiting value for increasing lateral dimensions of the island and the film (Figure 5b). On a heterogeneous surface, the full polarization height of a feature and hence the true value of the dielectric constant of this feature is measured only once its lateral extent is large enough such that  $v\tau/l << 1$ . Figure 5b shows that flat-top islands of 1.0-nm topographic heights have polarization heights of  $-6 \text{ nm}$  when 400-nm wide,  $-9 \text{ nm}$  when 800-nm wide, and a final value of  $-10 \text{ nm}$  when 1200-nm wide and larger. This empirical observation of 1200 nm is consistent with the condition  $v\tau/l << 1$  for  $v$  of  $11 \mu\text{m s}^{-1}$  and  $\tau$  of 10 to 30 ms at 80% RH. The observation is also consistent with the 300-nm length required for the full rise of the polarization height (Figure 5a): the tip should therefore have 300 nm of homogeneous material to its left and to its right to measure the full polarization height, coming to a total of 1200 nm when the left and right lateral rises are also included. When the condition  $v\tau/l << 1$  is not satisfied, as for the polarization heights more positive than  $-10 \text{ nm}$ , the scanning tip is not located over the surface feature for a sufficiently long time period to measure accurately the full polarization height. When  $l$  is too small, the apparent local dielectric constant is therefore a convolution of the dielectric constants of the substrate and of the feature.

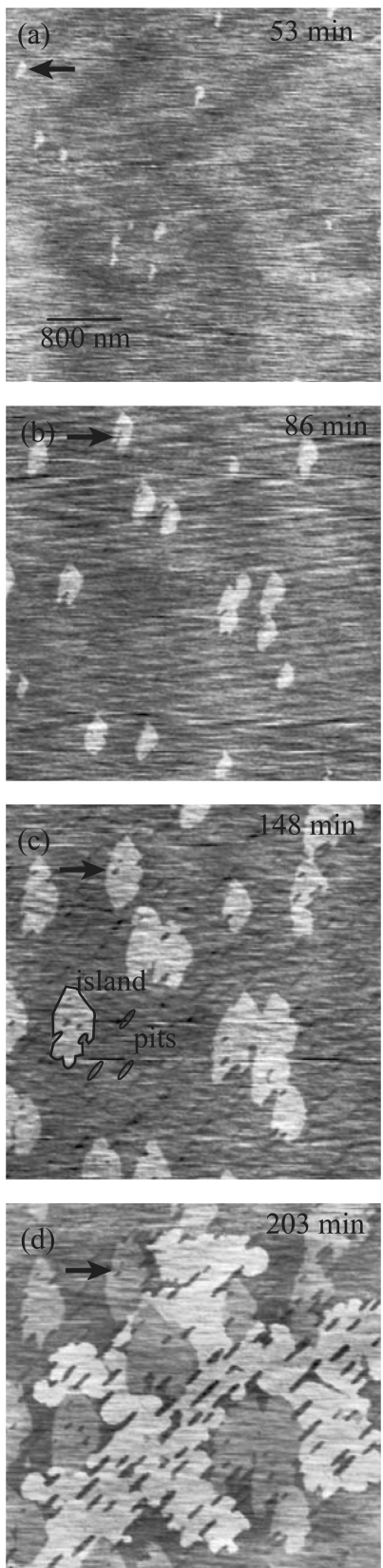


**Figure 2.** Time sequence of topographic images ( $4 \times 4 \mu\text{m}^2$ ) of the calcite surface at 80% RH. Shading is scaled to 4 nm. The image area shifts 0.5  $\mu\text{m}$  downward during the time series. The white arrow in each image indicates the same island. (a–c) Surface reconstruction during 150 min occurs by the nucleation and the growth of islands and by surface pitting. (d) A contiguous and rapidly growing film (light-colored) covers 35% of the scan area within 40 min. Neither the islands nor the contiguous film grows over the pits. As a result, the pits are more apparent in the later images.

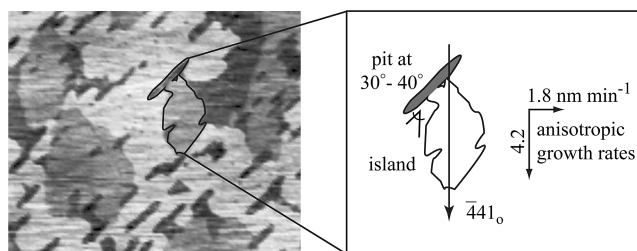
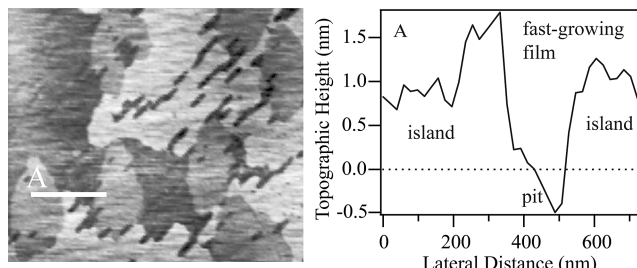


**Figure 3.** (top) Lateral and vertical dimensions of the reconstruction features (topographic images of  $2.2 \times 2.2 \mu\text{m}^2$ ). (bottom) Influence of substrate crystallography on the orientation of the islands and the pits. Crystallographic directions of the substrate are based upon large rhombohedral pits generated during cleavage and lying outside of the shown scan area. Shading in the top and bottom images is scaled to 3 nm.

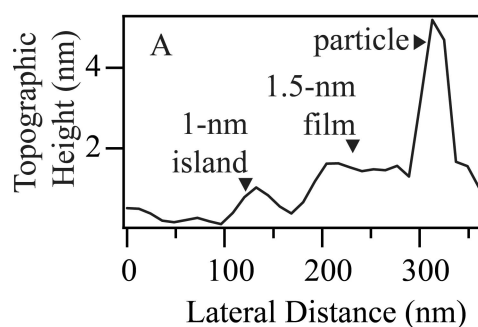
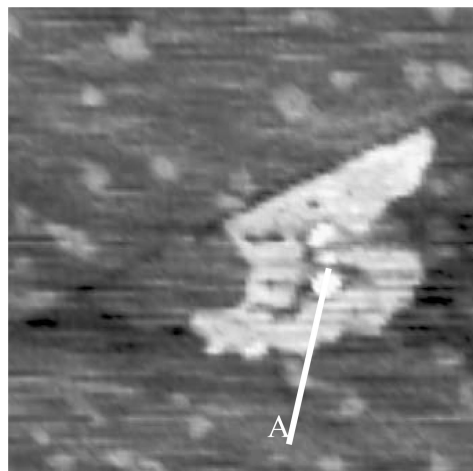


**Figure 4.** Rapid and contiguous film growth occurs near a 5-nm particle, which is a residual remaining after cleavage and preparation. The height image is collected at 80% RH (contact mode,  $965 \times 965 \text{ nm}^2$ ). The topographic height of the film around the particle is 1.5 nm. Film growth does not proceed across the 0.5-nm step apparent in the image. The topographic height of the islands is 1.0 nm.

The islands and the film have negative polarization heights (Figure 5a). The implication (vida infra) is that  $\epsilon(\hat{p}_{\text{substrate}}) > \epsilon(\hat{p}_{\text{film}}) > \epsilon(\hat{p}_{\text{island}})$  at 80% RH, where  $\hat{p}_{\text{island}}$  denotes when the tip is positioned above the  $x-y$  domain of an island. The domains of  $\hat{p}_{\text{film}}$  and  $\hat{p}_{\text{substrate}}$  are analogously defined. The

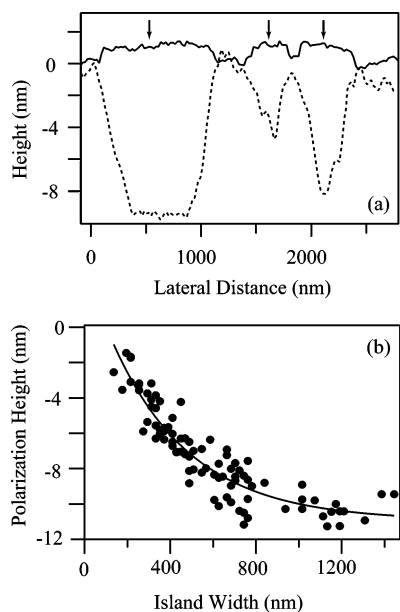


**Figure 5.** Lateral and vertical resolution of polarization-force microscopy. (a) Cross sections comparing topographic (solid line) and polarization (dashed line) heights of three flat-top islands (indicated by arrows). Although the topographic heights of the three islands are the same, the polarization heights depend on the lateral widths of the islands. The lateral length corresponding to the full vertical rise is approximately 50 nm for the topographic profile compared to 300 nm for the polarization profile. (b) Polarization height obtains one e-fold of its limiting value for 400-nm-wide islands. Part b is obtained by analysis of 60 cross sections of the type shown in part a. In this analysis, the topographic heights of the islands, which do not vary significantly, are represented by the cross section shown in part a.

conclusion regarding the rank ordering of  $\epsilon$  is reached as follows. The polarization heights of the islands and the contiguous film are  $-8$  to  $-10$  nm and  $-4$  to  $-5$  nm, respectively, compared to their respective topographic heights of  $+1.0$  and  $+1.5$  nm (Figure 6; case d of Figure 1). The heights are measured over islands and regions of the film having a significant enough lateral extent to satisfy  $v\tau/l \ll 1$ . A substantive contribution of the local contact potential to the polarization heights is ruled out, because the polarization contrast in the images is unchanged for a switch from a negative to a positive tip bias (data not shown). Moreover, the topographic heights are small compared to the polarization heights (e.g., accounting for  $+1.0$  nm of the polarization height of  $-10$  nm). When combined, these observations lead to the conclusion that changes in the local dielectric constant must account for the variations in the polarization heights (images a1 and b1 of Figure 6). Moreover, the rank ordering of the polarization heights shown in the cross section of image b1 implies that  $\epsilon(\hat{p}_{\text{substrate}}) > \epsilon(\hat{p}_{\text{film}}) > \epsilon(\hat{p}_{\text{island}})$ . Using Hook's law in conjunction with eq 1b, we estimate that the dielectric constant of the islands is 35% to 65% smaller than that of the film based upon their respective polarization heights. A similar rank ordering is also implied for the induced net cation-anion charge balance  $Q(\hat{p}_{\text{tip}})$  below the tip because the dielectric constant is nearly completely determined by ions for our experimental conditions.

Although differences in  $\epsilon(\hat{p})$  over an island or a film compared to the substrate result in principle both from changes in the molecular dipoles residing within the volume of the islands and the film and from changes in the density and the mobility of surface ions, three factors lead to an overall dominant contribution from the behavior of the mobile ions.<sup>15</sup> First, at a tip-sample separation distance of tens of nanometers, the nanometer-thick islands and films are not sufficient for a substantial

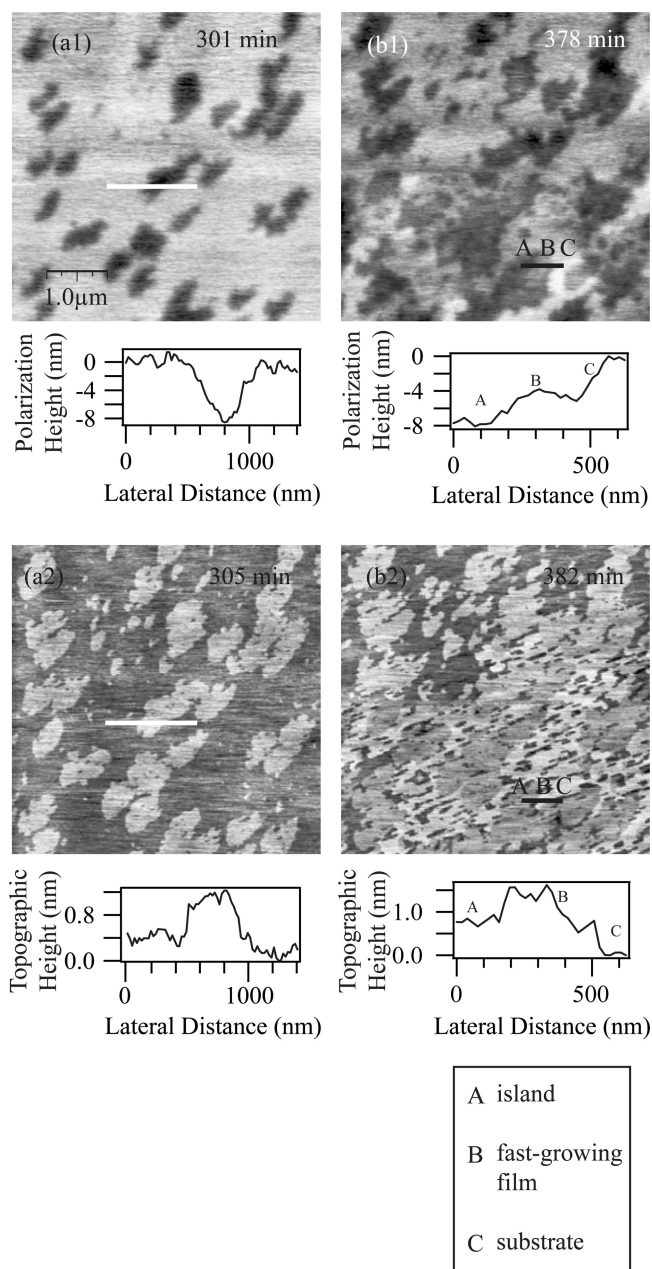


**Figure 6.** (a1 and b1) Polarization images of a reconstructing calcite surface after 301 and 378 min ( $5 \times 5 \mu\text{m}^2$ ,  $-3.0$  V tip bias, 80% RH). By 301 min, significant reconstruction occurs. By 378 min, a contiguous and rapidly growing film, which is similar to that shown in Figure 2d, extensively covers the initial surface. (a2 and b2) Topographic images of the same location as in a1 and b1 recorded 4 min after those polarization images. The islands in the topographic image of a2 appear as basins in the polarization images of a1. The cross sections of a1 and a2 show that the islands of 1.0-nm topographic height have a polarization height of  $-8$  nm. In comparison, the cross sections of b1 and b2 show that the film of 1.5-nm topographic height has a polarization height of  $-4$  nm.

molecular-dipole effect that can mask the underlying substrate.<sup>15</sup> Second, the sharp AFM tip allows for a small sampling area on the surface because of the focusing of field lines,<sup>15,22</sup> an effect which is accounted for in the tip-sample geometry function  $f(R/d)$ . Third, in a small sampling area, an ion cloud having a significantly unbalanced count of anions and cations develops as  $Q(\hat{p}_{\text{tip}})$ . This charged cloud dominates the dielectric constant compared to molecular dipoles. Focused field lines and locally unbalanced charge lead to a large polarization force.

There is an important empirical check that  $\epsilon(\hat{p})$  principally arises from the behavior of mobile surface ions for our experimental conditions at 80% RH. Upon the basis of the surface-averaged maximum repulsive polarization force (described by Kendall and Martin<sup>9</sup>), the mobile ions have a response time of 10 to 30 ms at 80% RH for a tip-biased ac at 7 Hz (data not shown). The force abruptly falls below the detection limit when the ac frequency is increased above 10 kHz. The mobile ions no longer have sufficient time to respond to the tip, and polarization arises only from molecular dipoles.<sup>23,24</sup> The molecular-dipole contribution to the dielectric constant, however, is so weak that the maximum polarization force falls below the detection limit. The conclusion is again reached that the density and mobility of surface ions is the quantity regulating the dielectric constant and hence the strength of the polarization force.

Figure 6 shows empirically that the lateral resolution in the polarization images is lower than in the corresponding contact images. Contributing factors limiting resolution in the polarization images are the tip-sample geometry function  $f(R/d)$ , the tip speed, and the polarization-force response time (see further in section on Relationship of  $\epsilon(\hat{p})$  to  $\sigma(\hat{p})$  and  $\mu(\hat{p})$ ).<sup>21</sup> The lateral resolution in the polarization images, which is approximately 50 nm in Figure 6, is regulated by a minimum detection sensitivity, which is a weaker condition than the measurement of the full polarization height (e.g., requiring homogeneous lateral features of 1200 nm in our study). The vertical resolution for the polarization and contact images is limited by the feedback loop in relation to the noise floor. In practice, vertical resolution is 0.3 nm for the polarization heights compared to 0.05 nm for the topographic heights.

**Relationship of  $\epsilon(\hat{p})$  to  $\sigma(\hat{p})$  and  $\mu(\hat{p})$ .** The relationship of the local dielectric constant  $\epsilon(\hat{p})$  to the local mobile-ion density  $\sigma(\hat{p})$  and to the local ion mobility  $\mu(\hat{p})$  is derived for  $v\tau/l \ll 1$ , as follows. An applied electric field resulting from a bias on the tip induces a local dielectric constant  $\epsilon$

$$\frac{\epsilon}{\epsilon_0} = 1 + \chi \quad (2)$$

where  $\chi$  is the electric susceptibility and  $\epsilon_0$  is the permittivity of free space. Migration of mobile ions in the applied electric field results in a net charge  $Q$  beneath the tip, leading to  $\chi = O(Q)$ , where  $O$  expresses the order of the functional dependence (i.e.,  $\chi$  is proportional to  $Q$ ).

The local steady-state value of  $Q$  in the ionic cloud depends on the local mobile-ion density  $\sigma$  and the local mobile-ion response time  $\tau$ . As a good approximation,  $Q$  approaches a steady-state value as a first-order process so that we can write

$$\frac{\epsilon}{\epsilon_0} = 1 + O\{\sigma[1 - \exp(-\tau_m \tau^{-1})]\} \quad (3)$$

where  $\tau_m$  is the sampling time of the measurement (i.e., a characteristic dwell time). The combination of a tip speed of 11  $\mu\text{m s}^{-1}$  and an observed lateral resolution of 50 nm suggests that the sweeping tip carries with it across the surface an ion cloud whose main constituents have migrated on average for 4.5 ms, which serves as an approximate value of  $\tau_m$ . In comparison, the  $\tau$  required for the migrating ions to reach their steady-state positions below a stationary tip is between 10 and 30 ms for our experimental conditions at 80% RH.

Ion mobility  $\mu$  can be related to  $\tau$ , as follows. The steady-state  $Q$  beneath the tip arises from cation and anion diffusion in response to the electrochemical-potential gradient caused by

the biased tip. The result is  $\tau = O(\mu^{-1})$  by recalling the Einstein relation of  $D$  to  $\mu$  that  $D = O(\mu)^{25}$  and the solution of Fick's laws that  $\tau = O(D^{-1})$ ,<sup>25</sup> where  $D$  is the diffusion coefficient in the  $x-y$  plane. Motion in the  $z$ -direction is negligible due to the thinness of the water layer.

Image contrast derives from the change  $\Delta\epsilon$  of the dielectric constant compared to the baseline setpoint over the substrate. The quantity  $\Delta\epsilon_{i/s}$  over an island compared to the substrate can be calculated from eq 3 with the substitution  $\tau^{-1} = O(D)$ , as follows:

$$\Delta\epsilon_{i/s} = \epsilon_0 [O[\sigma_{\text{island}}\{1 - \exp[-\tau_m O(\mu_{\text{island}})]\} - \sigma_{\text{substrate}}\{1 - \exp[-\tau_m O(\mu_{\text{substrate}})]\}]] \quad (4)$$

An analogous relationship exists for the change in dielectric constant  $\Delta\epsilon_{f/s}$  of the film compared to that of the substrate. ( $\sigma_{\text{island}}$  is the same as  $\sigma(\hat{p}_{\text{island}})$ , where the former notation is used in eq 5 for clarity of presentation.)

Equation 4 can be further developed by considering two limiting cases. Case I assumes a slow tip speed (i.e.,  $\tau_m \gg \tau$ ), which leads to the simplification that  $\Delta\epsilon_{i/s} = \epsilon_0 O(\sigma_{\text{island}} - \sigma_{\text{substrate}})$ . Under this condition, the polarization height measures the difference in the density of mobile ions over the islands compared to that over the substrate. The same result derives by assuming that  $\mu(\hat{p}_{\text{substrate}}) = \mu(\hat{p}_{\text{island}})$ . In Case I, the observation  $\epsilon(\hat{p}_{\text{substrate}}) > \epsilon(\hat{p}_{\text{island}})$  would imply  $\sigma(\hat{p}_{\text{substrate}}) > \sigma(\hat{p}_{\text{island}})$ . A lower mobile-ion density over the islands could arise from a decreased kinetic or thermodynamic propensity to release ions into an adsorbed water layer or alternatively a decreased thickness of the adsorbed water layer.

Case II assumes that  $\sigma(\hat{p}_{\text{substrate}}) = \sigma(\hat{p}_{\text{island}})$ . Under this condition, the polarization height responds to the change in the mobility of the ions over each material, as quantified by the following equation:

$$\Delta\epsilon_{i/s} = \epsilon_0 \sigma O\{\exp[-\tau_m O(\mu_{\text{substrate}})] - \exp[-\tau_m O(\mu_{\text{island}})]\} \quad (5)$$

The observation  $\epsilon(\hat{p}_{\text{substrate}}) > \epsilon(\hat{p}_{\text{island}})$  would imply  $\mu(\hat{p}_{\text{substrate}}) > \mu(\hat{p}_{\text{island}})$ . A lower ion mobility over the islands could arise from a favorable interaction between the mobile ions and the structural elements of the island. A decreased water-layer thickness over the islands could also reduce the level of ion hydration and thus mobility.

Our observations in Figures 5–8 cannot be simplified to either limiting case. The analysis does show, however, that the observation  $\epsilon(\hat{p}_{\text{substrate}}) > \epsilon(\hat{p}_{\text{film}}) > \epsilon(\hat{p}_{\text{island}})$  is consistent with a hypothesis of a similar rank order in water layer thickness.

**Effect of Relative Humidity on Surface Reconstruction.** The effect of relative humidity, which is a surrogate for the amount of surface-associated water, is explored (Figure 7). The time course of surface reconstruction at 80% RH is shown in Figure 2. At 50% RH, surface reconstruction proceeds in a qualitatively similar manner but at a much slower rate (images not shown). At 20% RH, no reconstruction is observed during 9 h. Our previous polarization-force measurements on calcite<sup>9</sup> suggest that the water film coverage below 60% RH is less than a monolayer, implying that the ions lack sufficient solvation to overcome the activation energies necessary for rapid surface motion.

The following evidence suggests that the chemical constituents of the islands are in reversible equilibrium with the adsorbed water, thus implying dynamic exchange of water molecules. Islands are initially grown at 80% RH, and the relative humidity is then decreased stepwise to 8%. The topographic heights of

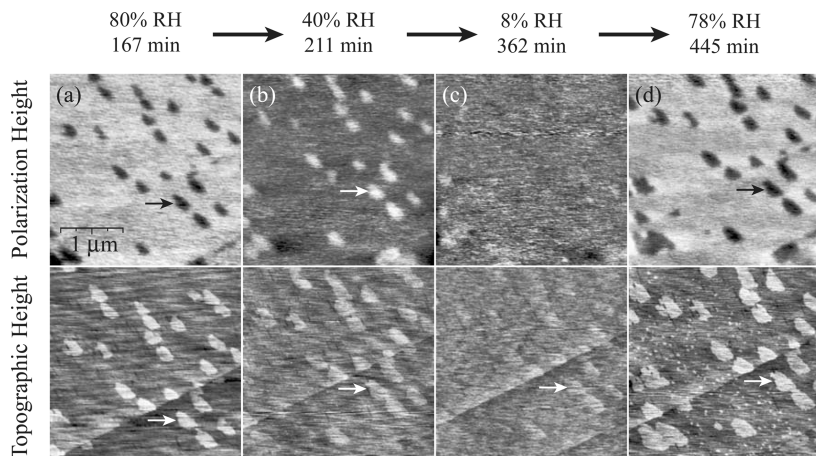


**Figure 7.** Film properties depend on relative humidity. Polarization and topographic images are shown for a program of 80% → 40% → 8% → 78% RH (images of  $3 \times 3 \mu\text{m}^2$ ; tip bias of  $-3.0 \text{ V}$  for the polarization images). The arrow points to the same island in each image. (a and b) The contrast reverses in the polarization images for a drop in the relative humidity from 80% to 40%. The polarization heights of the islands are negative at the high relative humidity but positive at the low relative humidity. (c) For 8% RH, contrast in the polarization image is lost. (d) Restoration to 78% RH provides an image that is similar to that of a, a finding which demonstrates an absence of hysteresis during RH cycling, at least for this specific type of observation. The topographic images in the lower row of a through d show that the heights of the islands decrease at lower relative humidities (see also Figure 8). Although the topographic height of the islands depends on RH, the topographic height of a nearby terrace step does not, at least within the uncertainty of the measurement.

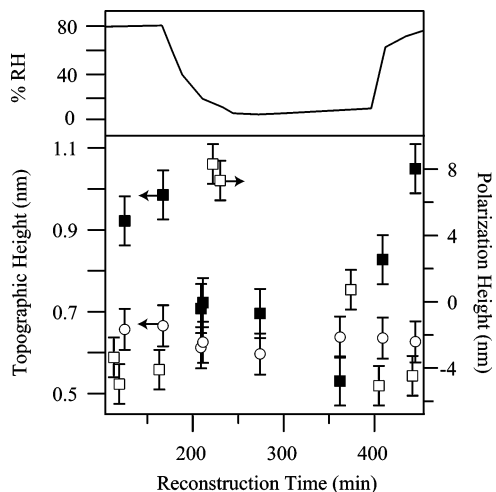


**Figure 8.** Topographic and polarization heights of islands at different relative humidities. Closed squares (■) represent the average topographic heights of multiple islands. Open squares (□) represent the average polarization heights of multiple islands. Also shown by circles (○) are the average step heights of multiple measurements along the same step. The standard deviations shown in the figure correspond to the  $2\sigma$  distribution of 10 measurements at each time point.

The islands shown in Figure 7 decrease from 1.0, to 0.7, to 0.5 nm for drops in RH from 80%, to 40%, to 8%, respectively. In contrast, the topographic heights of the substrate steps do not depend on RH (Figure 8). The dependence of island height on RH, therefore, is not an artifact of imaging at low relative humidity (e.g., changes in meniscus forces). These observations indicate that the structures of the islands depend on the quantity of surface-adsorbed water. Moreover, these islands are in dynamic equilibrium of dissolution and growth because no hysteresis is observed: increasing from 8% to 80% RH restores the topographic island height to 1.0 nm.

In contrast to the monotonic decrease in topographic height for drops in RH, the polarization heights of the islands have a more complex behavior. They change from negative to positive, corresponding to a change from case d to b of Figure 1, for a drop from 80% to 60% RH. In both cases, however, the magnitude of the polarization heights exceeds that of the topographic heights (i.e.,  $-5 \text{ nm}$  compared to  $1.0 \text{ nm}$  at 80%

RH and  $+8 \text{ nm}$  compared to  $0.7 \text{ nm}$  at 60% RH). The behavior from 60% to 8% RH is qualitatively similar to that of 60% (Figure 8). Below 8% RH, the polarization height is equal to the topographic height, at least within the measurement uncertainty of the SPFM technique (see section on Local Dielectric Constant  $\epsilon(\hat{p})$ ) (Figure 7c).

The magnitude of polarization heights at different RH values (e.g.,  $-5 \text{ nm}$  at 80% RH and  $+8 \text{ nm}$  at 60% RH) must not be compared because the sensitivity of the measurement changes. Specifically, the tip–sample separation required for stable imaging decreases for decreasing RH value: the decrease in the mobility and the density of surface ions at low RH values implies that the local dielectric constant decreases and thus that the tip must be brought closer to the surface to satisfy the imaging setpoint. Equation 1b shows that an increase in  $f(R/d)$  and a decrease in  $\epsilon$  affect  $\partial_\epsilon F$ . For example, for a fixed  $\Delta\epsilon$  and all other factors equal,  $\partial_\epsilon F$  increases if  $f(R/d)/(\epsilon + 1)^2$  increases, which is the case suggested by our observations.

Although the change in magnitude for a drop from 80% to 60% RH depends on instrumental factors, the change in sign from negative to positive implicates changes in the properties of the islands and the substrate. A reverse in the sign of the polarization height under low RH conditions could arise from (1) a change of sign in  $\Delta\epsilon_{i/s}$  of eq 5, because  $\sigma(\hat{p}_{\text{substrate}})$  decreases more than  $\sigma(\hat{p}_{\text{island}})$  or because  $\mu(\hat{p}_{\text{substrate}})$  decreases more than  $\mu(\hat{p}_{\text{island}})$  for a drop in RH or (2) a relaxation in the simplification that the contribution of  $\partial_\epsilon F$  is small compared to the dielectric term  $\partial_\epsilon F$ . The first possibility, although it cannot be entirely ruled out, can be argued as not physically realistic under a model that  $\sigma$  and  $\mu$  are linear in water-layer thickness. In contrast, in relation to the second possibility, the force at a fixed tip–sample separation decreases for a drop in RH (data not shown), which implies a decreasing dielectric contribution to the polarization force and hence an increasing relative importance of the contact-potential contribution. As the surface dries,  $\epsilon$  is expected to decrease monotonically because of reduced mobility and density of surface ions, whereas fixed surface charge, which gives rise to  $\varphi$ , remains constant. Islands having positive polarization heights are expected provided that  $\varphi(\hat{p}_{\text{substrate}}) < \varphi(\hat{p}_{\text{island}})$  for a negative tip bias and positive  $\varphi$ . In line with this reasoning of

a positive  $\varphi$ , at even lower RH the tip cannot be successfully engaged when a positive instead of a negative bias is employed.

**Proposed Chemical Composition of Islands.** We propose that the islands are composed of a loosely bound hydrate structure of calcium carbonate. The behavior of the islands in response to varying relative humidity and hence to varying amounts of adsorbed water supports this proposal. Specifically, for decreasing relative humidity, the topographic height of the islands decreases to 0.5 nm, whereas for increasing relative humidity, it increases to up to 1 nm. The dependence of film height on water-surface coverage is evidence that loosely bound water is a chemical constituent of the islands. Moreover, infrared evidence shows that a quantity of water equivalent to two to four monolayers is present on the calcite surface at 80% RH,<sup>26</sup> corresponding to a height of 0.2 to 0.4 nm. The 0.5-nm drop in island height for a decrease from 80% to 8% RH is an equivalent amount of water. A labile structure such as we are proposing could also be anticipated to be mechanically delicate. In this regard, the setpoint force in contact mode can be increased beyond a threshold value of 12 nN such that the islands are destroyed or displaced by the scanning tip (data not shown).

Hydrated calcium carbonate is a bulk solid that is widely used by organisms in the processes of biomineralization,<sup>1</sup> although it is thermodynamically metastable and lacks the long-range atomic ordering of calcite or its polymorphs. In our study of thin islands, however, the underlying substrate may provide stabilizing interfacial energy so that the thin-film hydrated phase is thermodynamically stable.<sup>27</sup> The orientation of the islands relative to the substrate also suggests the presence of crystallographic order within the atomic structure of the islands (Figure 3). There are thus two important differences between the proposed hydrate structure of the islands and the known properties of bulk, amorphous hydrated calcium carbonate.

Mass balance requires a source of the  $\text{CaCO}_3$  material constituting the islands. Material becomes available from the nucleation and growth of surface pits, from the dissolution of large particles formed during cleavage and remaining after cleaning, and from the retreat of multilayer steps on the substrate.  $\text{Ca}^{2+}$  and  $\text{CO}_3^{2-}$  ions released in these processes are mobilized in the adsorbed water layer and can diffuse and attach to the expanding edges of the islands.

## Conclusion and Implications

The results of this study show that reconstruction of a cleaved calcite surface in humid air is dominated by film growth, including both a patchy island network and a contiguous film. Mass transfer occurs among many surface elements, including islands and pits on the substrate, macroscopic and microscopic  $\text{CaCO}_3$  particles produced by cleavage, and ions in the surface-adsorbed water layer. The results provide a detailed, quantitative characterization of film growth, including lateral and vertical dimensions, lateral and areal growth rates, and crystallographic orientation of the islands relative to the substrate. Polarization measurements at 80% RH show that the dielectric constant over the substrate is greater than that over the film, which suggests that either or both the density and the mobility of surface ions are correspondingly lower in the water layer over the film. Application of this technique to study the properties of surface-adsorbed water and ions holds potential to provide future insights in areas such as corrosion studies,<sup>28</sup> advances in friction, adhesion, and lubrication,<sup>29,30</sup> and technologically focused studies of thin film growth and function.<sup>31</sup>

The results of the current work provide several lines of evidence in support of hydrated calcium carbonate as the island

material. Hydrated calcium carbonate is widely understood to require the co-presence of organic materials, such as lipids and proteins,<sup>1,32</sup> to inhibit rapid recrystallization. The results of this work, however, suggest that hydrated calcium carbonate could also be stable in inorganic systems having a favorable match to the underlying calcite substrate.

Minerals in natural and model systems often have important sample-to-sample differences in surface properties, including reactivity. Molecular relaxation and reconstruction at surfaces have been investigated by structural studies using synchrotron-based techniques. The results of the present work point out that film growth is clearly another important pathway leading to differences among the properties of calcite surfaces in natural and model systems. Sample history, therefore, is important in determining reactivity. Samples aged under humid conditions may be covered by films having lower ion densities and mobilities compared to samples aged under dry conditions.

Transformation of the hydrated calcium carbonate film to another phase is possible over long times.<sup>33–35</sup> Possible phases for the  $\text{CaCO}_3\text{-H}_2\text{O}$  system of this study include metastable calcite polymorphs such as aragonite as well as the stable end-member calcite. In more complex, multicomponent environmental systems, phase transformations during aging could provide pathways for the incorporation of foreign divalent metals, such as  $\text{Mg}^{2+}$  and  $\text{Cd}^{2+}$ . The foreign ions could diffuse into the labile hydrate structure and could become locked in place upon an abrupt phase transition. This proposed pathway could circumvent energetically unfavorable and slow solid-state diffusion. Possible stable phases for hydrate transformations in these environmental systems could then include Mg-calcite ( $\text{Ca},\text{Mg}\text{CO}_3$ ), otavite  $\text{CdCO}_3$ , and dolomite  $\text{CaMg}(\text{CO}_3)_2$ , provided that sufficient amounts of magnesium or cadmium are present.

**Acknowledgment.** We are grateful for support received from the Petroleum Research Fund and the Chemical Sciences, Geosciences, and Biosciences Division of the Office of Basic Energy Sciences in the U.S. Department of Energy.

**Supporting Information Available:** Two AFM movies (S1 and S2) show calcite surface reconstruction under humid air. S1 is a time sequence of AFM contact-mode micrographs ( $5 \times 5 \mu\text{m}^2$ ,  $-3.0$  V tip bias, 80% RH) of the reconstructing calcite surface where reconstruction is characterized by island growth and pit formation. S2 is a time sequence of AFM contact-mode micrographs ( $5 \times 5 \mu\text{m}^2$ ,  $-3.0$  V tip bias, 80% RH) showing the appearance of the fast-growing, 1.5-nm-high film after 200 min. This material is available free of charge via the Internet at <http://pubs.acs.org>.

## References and Notes

- (1) Addadi, L.; Raz, S.; Weiner, S. *Adv. Mater.* **2003**, *15*, 959.
- (2) Stumm, W.; Morgan, J. *J. Aquatic Chemistry*; Wiley: New York, 1996.
- (3) Klein, C.; Hurlbut, C. S. *Manual of Mineralogy*, 21st ed.; Wiley: New York, 1993.
- (4) Sposito, G. *The Chemistry of Soils*; Oxford University Press: New York, 1989.
- (5) Rivadeneyra, M. A.; Delgado, R.; Delgado, G.; Delmoral, A.; Ferrer, M. R.; Ramoscormenzana, A. *Geomicrobiol. J.* **1993**, *11*, 175.
- (6) Krueger, B. J.; Ross, J. L.; Grassian, V. H. *Langmuir* **2005**, *21*, 8793.
- (7) Krueger, B. J.; Grassian, V. H.; Laskin, A.; Cowin, J. P. *Geophys. Res. Lett.* **2003**, *30*, 1148.
- (8) Adamson, A. W. *Physical Chemistry of Surfaces*, 5th ed.; Wiley: New York, 1990.
- (9) Kendall, T. A.; Martin, S. T. *Geochim. Cosmochim. Acta* **2005**, *69*, 3257.
- (10) Stipp, S. L. S. *Geochim. Cosmochim. Acta* **1999**, *63*, 3121.

- (11) Stipp, S. L. S.; Gutmannsbauer, W.; Lehmann, T. *Am. Mineral.* **1996**, *81*, 1.
- (12) Liang, Y.; Baer, D. R.; McCoy, J. M.; Amonette, J. E.; LaFemina, J. P. *Geochim. Cosmochim. Acta* **1996**, *60*, 4883.
- (13) Israelachvili, J. N. *Intermolecular and Surface Forces*, 2nd ed.; Academic Press: San Diego, 1992.
- (14) Diez-Perez, I.; Luna, M.; Teheran, F.; Ogletree, D. F.; Sanz, F.; Salmeron, M. *Langmuir* **2004**, *20*, 1284.
- (15) Xu, L.; Salmeron, M. *Nano Surf. Chem.* **2001**, *243*.
- (16) Xu, L.; Salmeron, M. *Langmuir* **1998**, *14*, 5841.
- (17) Dai, Q.; Hu, J.; Salmeron, M. *J. Phys. Chem. B* **1997**, *101*, 1994.
- (18) Hu, J.; Xiao, X. D.; Salmeron, M. *Appl. Phys. Lett.* **1995**, *67*, 476.
- (19) Morse, J. W.; Arvidson, R. S. *Earth Sci. Rev.* **2002**, *58*, 51.
- (20) Vansanten, R. A. *J. Phys. Chem.* **1984**, *88*, 5768.
- (21) Rieutord, F.; Salmeron, M. *J. Phys. Chem. B* **1998**, *102*, 3941.
- (22) Luna, M.; Rieutord, F.; Melman, N. A.; Dai, Q.; Salmeron, M. *J. Phys. Chem. A* **1998**, *102*, 6793.
- (23) Kasap, S. O. *Principles of Electronic Materials and Devices*; McGraw-Hill: Boston, 2001.
- (24) Xu, L.; Lio, A.; Hu, J.; Ogletree, D. F.; Salmeron, M. *J. Phys. Chem. B* **1998**, *102*, 540.
- (25) Atkins, P. W. *Physical Chemistry*, 3rd ed.; University Press: Oxford, 1988.
- (26) Al-Hosney, H. A.; Grassian, V. H. *Phys. Chem. Chem. Phys.* **2005**, *7*, 1266.
- (27) Jun, Y. S.; Kendall, T. A.; Martin, S. T.; Friend, C. M.; Vlassak, J. J. *Environ. Sci. Technol.* **2005**, *39*, 1239.
- (28) Dai, Q.; Hu, J.; Freedman, A.; Robinson, G. N.; Salmeron, M. *J. Phys. Chem.* **1996**, *100*, 9.
- (29) Weisenhorn, A. L.; Maivald, P.; Butt, H. J.; Hansma, P. K. *Phys. Rev. B* **1992**, *45*, 11226.
- (30) Persson, B. N. *J. Phys. Rev. B* **1993**, *48*, 18140.
- (31) Niesen, T. P.; De, Guire, M. R. *J. Electroceramics* **2001**, *6*, 169.
- (32) DiMasi, E.; Patel, V. M.; Sivakumar, M.; Olszta, M. J.; Yang, Y. P.; Gower, L. B. *Langmuir* **2002**, *18*, 8902.
- (33) Beniash, E.; Aizenberg, J.; Addadi, L.; Weiner, S. *Proc. R. Soc. London, Ser. B* **1997**, *264*, 461.
- (34) Aizenberg, J.; Lambert, G.; Addadi, L.; Weiner, S. *Adv. Mater.* **1996**, *8*, 222.
- (35) Brecevic, L.; Nielsen, A. E. *J. Cryst. Growth* **1989**, *98*, 504.